# The influence of hygrothermal aging on the fatigue behavior and residual strength of post-buckled co-bonded stiffened panels subjected to compressive loading

Bart P.H. van den Akker [a,b,*], Mauricio V. Donadon [a], Richard Loendersloot [b], Lucas A. de Oliveira [a], Mariano A. Arbelo [a]

[a] Department of Aeronautical Engineering, Instituto Tecnológico de Aeronáutica, Praça Marechal Eduardo Gomes 50, 12228-900, São José dos Campos, SP, Brazil
[b] Faculty of Engineering Technology, University of Twente, De Horst 2, 7522, LW, Enschede, The Netherlands

## ARTICLE INFO

## ABSTRACT

Adhesively bonded composite structures, if designed properly, have proven to be stiffer and to possess a higher specific strength than their mechanically fastened counterparts. To increase the applicability of these bonded joints in the aircraft industry, a study was performed to investigate the influence of hygrothermal aging on co-bonded composite stiffened panels with an initial disbond under cyclic compression loading. Experiments showed that hygrothermal aging led to a decrease in disbond growth throughout cyclic loading. The decreased disbond growth was likely caused by the increased ductility of the bond due to the presence of moisture. A higher ductility can lead to crack blunting and stress relaxation, resulting in higher fracture toughness of the bond. Furthermore, it was shown that hygrothermal aging did not influence the residual strength and stiffness of the panels after cyclic loading. The experiments were simulated numerically to gain a better understanding of the crack growth behavior and to aid future numerical crack growth predictions.

## 1. Introduction

Currently, a conservative design approach, such as safe life design, is often applied for bonded carbon fiber reinforced polymers (CFRPs) in primary aircraft structures. Primary aircraft parts made from aluminum have already shown that adapting to a damage tolerant design methodology can lead to significant weight reductions. Before this design methodology can be applied to CFRP parts, both the static and fatigue behavior of the bonded structures throughout their service life need to be fully understood.

The major part of an aircraft structure consists of sheet material, referred to as the skin, with stiffeners attached to it. Previous research on bonded CFRP in aircraft has mainly focused on these panel-like structures [1]. Especially the static buckling [1–3] and post-buckling [1, 3–13] of bonded stiffened panels have thoroughly been researched. These studies have demonstrated that stiffened panels are capable of taking on loads far beyond the initial buckling load. However, it has also been shown that the presence of an initial disbond can potentially lead to excessive disbond growth and premature failure of such structures [14].

Intuitively, one may argue that excessive disbond growth may become even more critical when panel-like structures are loaded cyclically. However, both Davila and Bisagni [15] and Abramovich and Weller [16] demonstrated that composite bonded panels can safely be taken into the post-buckling regime repeatedly.

Besides cyclic loads, aircraft have to endure environmental factors such as UV, moisture, temperature cycling and sometimes even fire [17–19]. Of these factors temperature effects and moisture are considered to be the most critical [18]. Currently, the combined effects of temperature and moisture have not yet been fully understood [18,20].

Although temperature and moisture effects are considered critical for the performance of a bond, no reference was found incorporating the influence of environmental effects on the long term behavior of bonded composite panels subjected to cyclic loads. The present study has aimed to fill this gap and to increase the knowledge of the performance of composite bonded joints. This can lead to an increase of the usage of bonded CFRP parts in aircraft structures.

This study has focused specifically on the influence of hygrothermal aging on stiffened CFRP panels with an initial disbond, subjected to compressive cyclic loading. The disbonded area was monitored
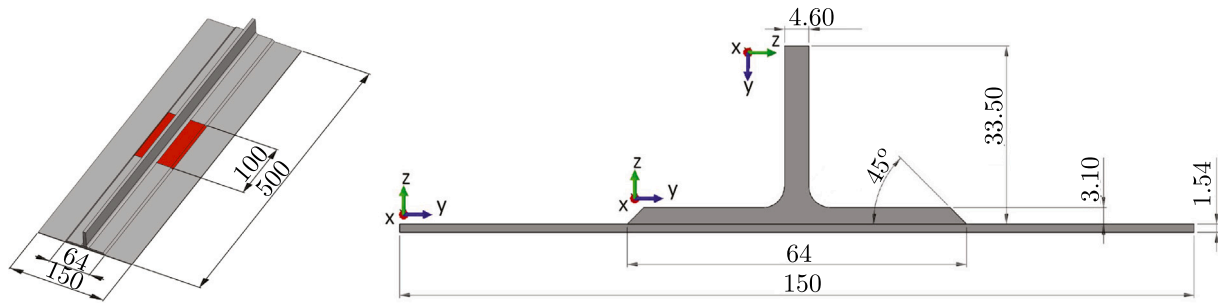
**Fig. 1.** Isometric view and front view of the panels. Teflon™ insert is depicted in red. All dimensions in *mm*. (For interpretation of the references to color in this figure legend, the reader is referred to the web version of this article.)

throughout the experiments to determine the influence of hygrothermal aging on the disbond growth. In addition, the residual strength of all cyclically loaded panels was determined and compared to the strength of non cyclically loaded reference panels. After the experimental part the cyclic disbond growth was simulated numerically using a fatigue damage model similar to the one proposed by Kawashita and Hallett [21], which has been given in detail in Ref. [22] Such a numerical simulation using explicit time integration has not previously been performed on sub-component level in the open literature. These numerical simulations will be a vital aspect in proving that the crack growth of cyclically loaded bonded parts can be predicted sufficiently accurate. This may eventually allow aircraft manufacturers to start using the slow crack growth approach as proposed by the FAA [23].

## 2. Materials and specimen preparation

### 2.1. Material and specimen configuration

Separate skins and stiffeners were manufactured out of T800/3900-2B carbon fiber epoxy using hand lay-up. A material data sheet of the carbon fiber epoxy and epoxy based adhesive are attached in Appendix A. The stiffener was pre-cured at 177 °C for 7 h. EA 9695 adhesive was then used to bond the stiffener to the skin and subsequently the materials were jointly cured at 177 °C for 7 h. Relevant material properties of the adhesive and interface layer can be found in Appendix A. An initial disbond was created by placing a 100 mm Teflon™ insert between the skin and stiffener before the second cure. The dimensions of the panels are given in Fig. 1 and the lay-up of the panels in Table 1.

### 2.2. Conditioning procedure

The hygrothermally conditioned panels were kept in an environmental chamber at 80 °C and 90% humidity for 280–396 days. These panels are referred to as Room Temperature Wet (RTW). The non aged panels are referred to as Room Temperature Ambient (RTA). Room temperature refers to the testing conditions.

Throughout the aging period the moisture content in the panels was monitored by following the ASTM D5229 [24] standard. This standard prescribes that the moisture uptake is equal to:

$$\phi = \frac{W_t - W_0}{W_0} \cdot 100\% \tag{1}$$

where $\phi$ is the moisture uptake as a percentage, $W_t$ is the weight of the panel at time $t$ and $W_0$ is the weight of the panel before conditioning. A representative moisture absorption curve is shown in Fig. 2. At the moment of testing all aged panels absorbed between 0.61% and 0.64% moisture. This was less than the 0.79% moisture at the saturation point of the same material combination during coupon level experiments as performed by Gonzalez et al. [25], indicating that moisture penetrates into smaller specimens more easily.
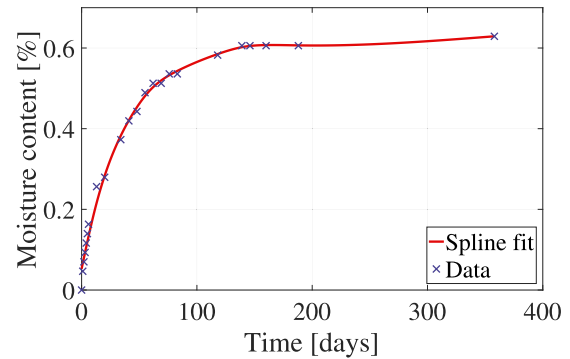


**Fig. 2.** Moisture absorption of panel 405–02 RTW.

## 3. Experimental procedure

The experimental phase consisted of two types of experiments, namely cyclic loading and quasi-static compression until failure. Eight panels were subjected to cyclic loading, during which the disbond size was measured regularly. The experimental set-up used during cyclic loading is explained in Section 3.1. After cyclic loading these same panels were subjected to quasi-static compression to determine their residual strength. The residual strength was compared with two reference panels, which were compressed until failure without cyclic loading. The experimental set-up of the quasi-static experiments is explained in Section 3.2.

To ensure that the disbonded area had been fully opened before the experiments started, all panels were pre-cracked using the seven point bending procedure as described by van Rijn and Wiggenraad [26]. Pre-cracking was required, because during curing of the panels pressure had caused some adhesive to flow from underneath the Teflon tape, connecting the skin and stiffener at the edges of the flange of the stiffener. Pre-cracking was stopped when the disbonded area had reached 100 mm, which was determined visually by the operators. Since this did not prove to be very precise, small differences in the disbond size between different panels could be noticed at the start of the experiments.

### 3.1. Cyclic loading

Three RTA and five RTW panels were subjected to 300,000 load cycles between −4.7 and −47.5 kN. During this procedure a frequency of 5 Hz was applied, which did not result in the material heating up. This was determined by the use of an infrared camera. Clamped boundary conditions were used at the loaded ends, complimented by simple support boundary conditions at the unloaded edges. The latter were used to avoid unwanted buckling at the edges of the skin. These boundary conditions can be seen in Fig. 3.

**Table 1**
Lay-up of the skin and stiffener. Ply degrees are with respect to the x-axis as displayed in Fig. 1.

|  | Skin | Stiffener base | Stiffener flange |
| --- | --- | --- | --- |
| Number of plies | 8 | 16 | 24 |
| Lay-up | $[45°/90°/-45°/0°]_s$ | $[45°/0°/-45°/90°/45°/90°/$ $-45°/0°]_s$ | $[45°/0°/-45°/90°/45°/90°/$ $-45°/0°/0°/-45°/90°/45°]_s$ |



**Fig. 3.** Boundary conditions of the panels.



**Fig. 4.** Testing rig. 1: clamped ends. 2: Linear variable differential transformer. 3: Anti-buckling supports. 4: Strain gauges, six in total.
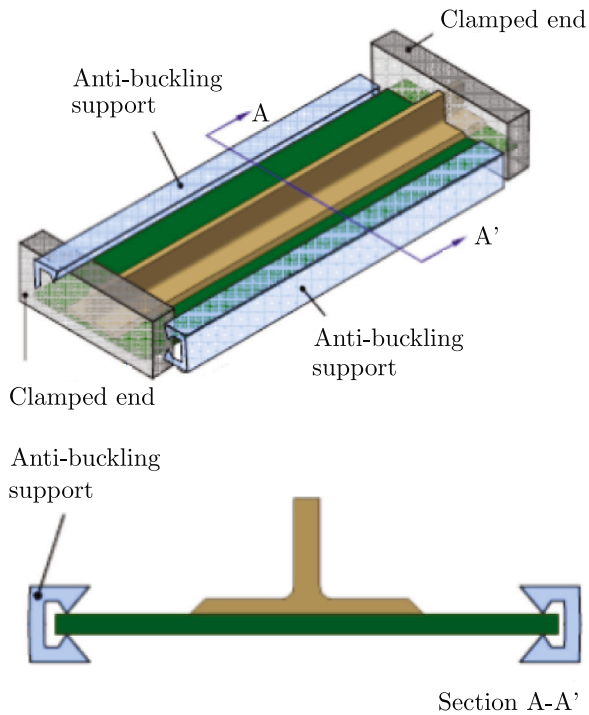
The testing rig is shown in Fig. 4. It has to be mentioned that the strain gauges shown in this figure have only been present during the quasi-static experiments, as their reliability during cyclic loading could not be guaranteed. Two pairs of strain gauges were placed back-to-back on the skin to determine the membrane and bending strains, needed for the characterization of the skin buckling load and further verification of the numerical model. The last two strain gauges were placed back to back on the stiffener. The Linear Variable Differential Transformer (LVDT) was used to determine the in-plane displacement, also referred to as the shortening.

The size of the disbonded area was measured after 0, 1, 500, 5000, 10,000, 30,000, 50,000, 100,000, 150,000, 200,000 and 300,000 load cycles. These measurements were performed by ultra-sound inspection using an Isonic 2006 produced by Sonotron NDT with a 5 MHz probe. To enable this the panels had to be dismounted and remounted from the testing rig. As it was assumed that all disbonding took place in the area surrounding the disbond-bond interface, only this area was inspected with ultrasound. After scanning, the results were post-processed in Matlab using a tool developed by Cederløff [27] to obtain the disbonded area.

The shortening of the panels, up to a load of −47.5 kN, was measured regularly to assess the global stiffness reduction of the panels. These load-shortening curves were constructed during the 1st cycle and after 500, 10,000, 50,000, 150,000 and 300,000 cycles. An increase in shortening can indicate intralaminar or translaminar damage. Both kinds of damage cannot be noticed by the ultra-sound scanning.
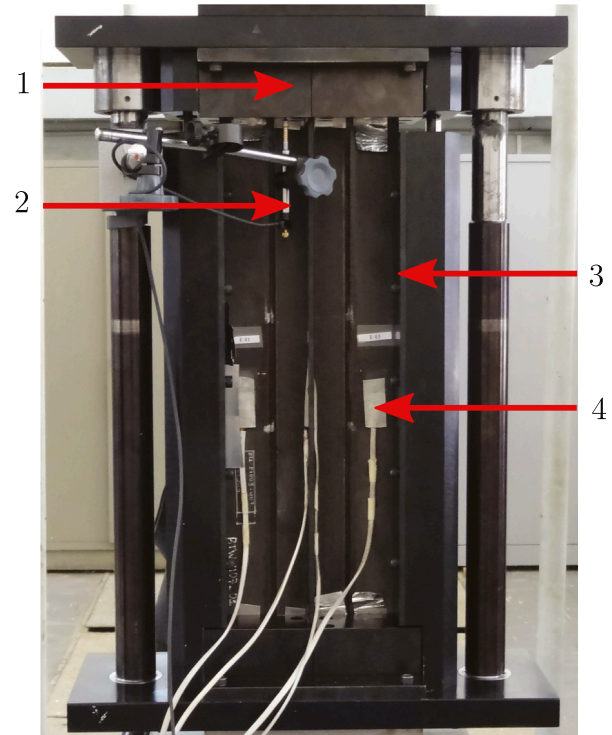
### 3.2. Quasi static compression

A load controlled Baldwin testing machine was used to load the panels under compression up to failure. The boundary conditions were similar to those during cyclic loading. Thereafter, the performance of the panels was determined by comparing buckling load, stiffness against compression and strength. The buckling load was calculated using the strain reversal method developed by NASA [28]. This method generally results in a conservative buckling load [29].

During the quasi-static loading of three panels Digital Image Correlation (DIC) was used to visualize the 2D buckling shape of the back side of the panel. Fig. 5 shows this DIC set-up. During the experiment pictures were taken at every −10 kN. These pictures were then post processed using ncorr V1.2 in Matlab to obtain the 2D displacement field [30]. It should be noted that the images acquired by the DIC can only be used in qualitative sense as a 3D DIC set-up is required to measure out-of-plane displacements correctly. A 3D DIC set-up was unfortunately not available during this research.

## 4. Results cyclic loading experiments

During the cyclic loading experiments the disbond size and stiffness of the panels were regularly monitored. The results of the former are discussed in Section 4.1 and the latter in Section 4.2.
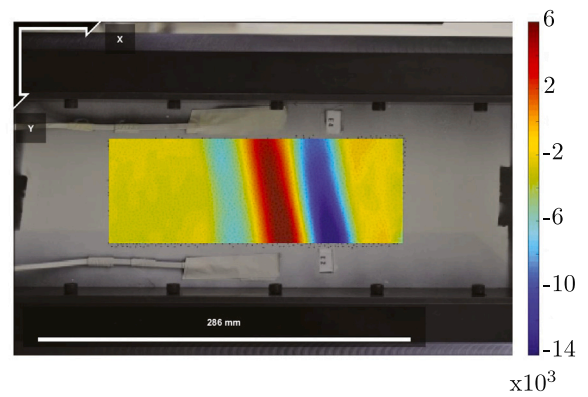
**Fig. 7.** Buckling shape of an RTA panel during the first load cycle at a load of −40 kN. This image can be used for qualitative comparisons only. The strains ($\mu\epsilon_{xx}$) are not representative because the out of plane displacements cannot be captured correctly by the 2D DIC set-up.

### 4.1. Disbond size

Fig. 6 shows the average growth of the disbond area throughout the cyclic loading experiments. To obtain this curve, the experimental data were averaged for both RTA and RTW panels. Subsequently, a power curve was used to fit the data, which resulted in the lowest Normalized Root Mean Square Error (NRMSE). Only the data from the first cycle and onward was considered in this fitting because, despite the pre-cracking, not all panels appeared to be fully opened before testing. After the first cycle all disbonds had been fully opened.

Significant was that the growth speed of the disbond area decreased as the amount of cycles increased. This cannot be distinguished directly from Fig. 6, due to the log-scale used on the *x*-axis, but can be retrieved from the exponents of the power fit being lower than unity: these exponents equal 0.1 and 0.24 for RTA and RTW respectively. The decrease in growth speed is most likely related to a decrease of stress concentrations in the corners of the bonded area. These stress concentrations were caused by the diagonal buckling shape as shown in Fig. 7. The buckling shape was diagonal due to the presence of ±45° layers on the outside of the skin. Repeated buckling then caused the disbonded area to grow diagonal as well, as shown in Fig. 8. As

a result, throughout cyclic loading, the disbonding area adjusted more and more to match the buckling shape. This caused the aforementioned decrease of stress concentrations in the highly stressed corners. This phenomenon occurred in both the RTA and RTW panels, resulting in similar disbond shapes at the end of the cyclic loading.

Throughout the cyclic loading the disbonded area of the hygrother-mally aged panels grew significantly less than the disbond of the RTA panels. Two factors have been identified that likely had contributed to this phenomenon:

1. Plasticization causing the propagation fracture toughness to increase.
2. The average disbonded area of the RTW panels being 4% larger than the RTA panels after the first cycle.

Considering the first point, it has been proven that moisture in adhesives causes plasticization [18,31,32]. Plasticization can lead to stress relaxation and is cited as a cause for the increased fracture toughness of bonded composite specimens after moisture exposure [31, 32]. Additionally, Packham [33] stated that plasticization causes crack blunting. A blunter crack tip leads to lower stress concentrations at the crack tip and thus less crack growth.

Regarding the second point, after one cycle, the RTW panels had a 4% larger disbond than the RTA panels. A numerical simulation, similar to the one discussed in Section 7, showed that this difference
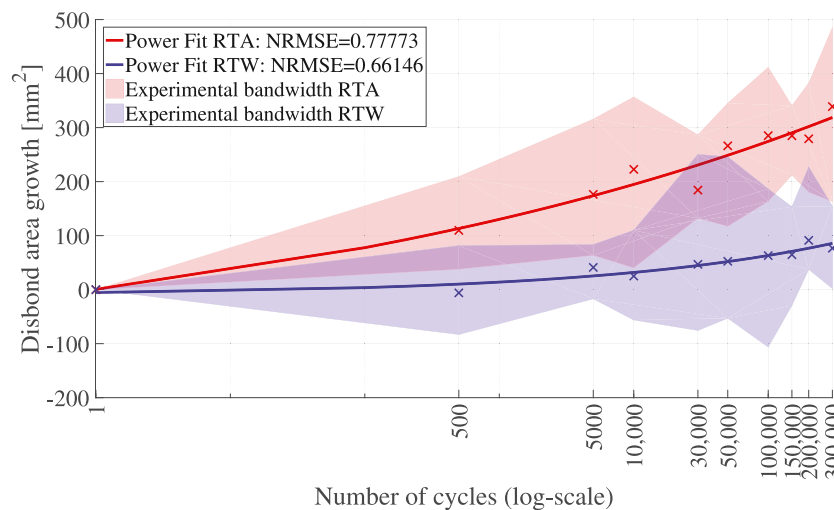


**Fig. 6.** Average growth of the disbonded area in the RTA and RTW panels.

(a) $N = 1$                                                    (b) $N = 300,000$
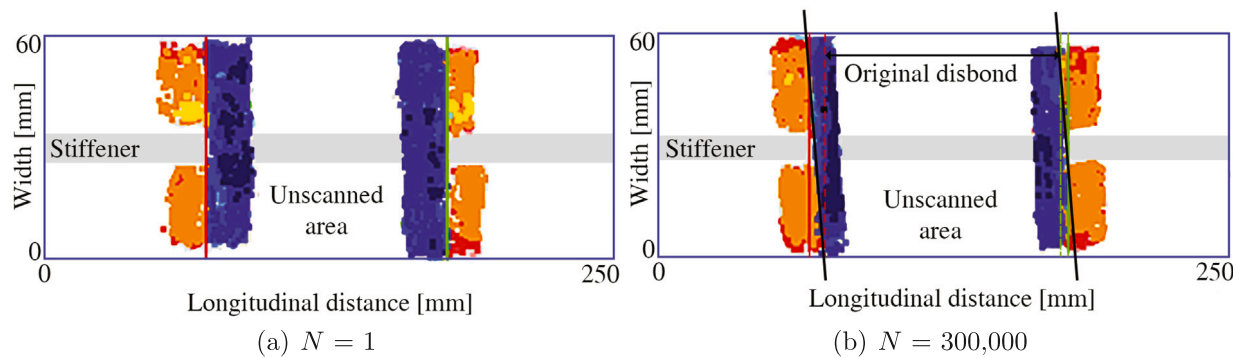
**Fig. 8.** Disbonded area (blue) and bonded area (orange/yellow) of panel 405–02 RTA after $N = 1$ and $N = 300,000$ cycles. Only the colored areas, around the disbond ends are scanned. The diagonal disbond growth in this panel is representative for both RTA and RTW panels. For illustrative reasons the web of the stiffener has been added in gray. (For interpretation of the references to color in this figure legend, the reader is referred to the web version of this article.)
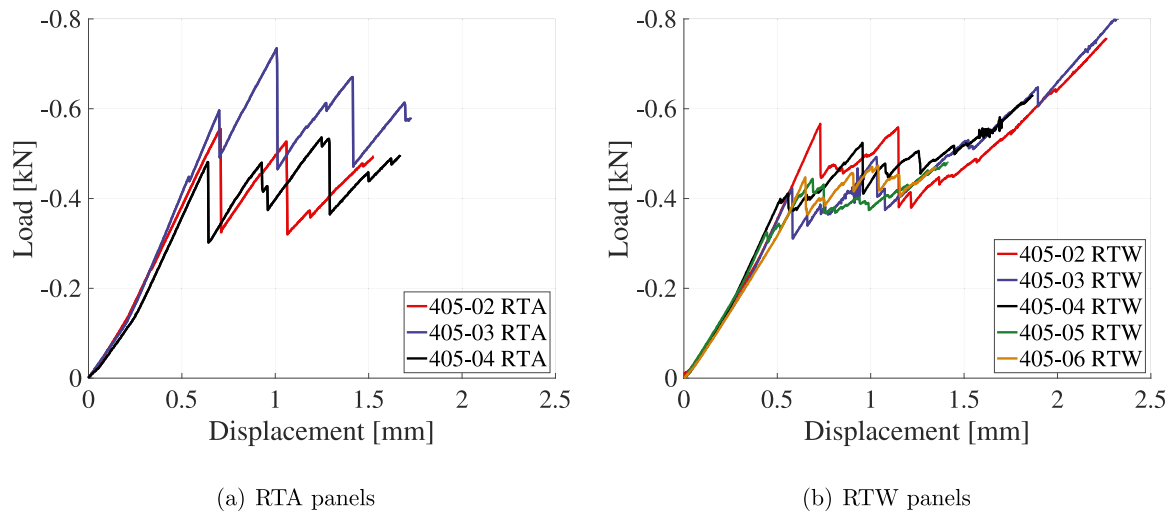


(a) RTA panels                                                    (b) RTW panels

**Fig. 9.** Load–displacement curves of the seven-point bending tests performed to pre-crack the panels.

can potentially cause a drop of up to 15% in disbond growth after 300,000 cycles.

The disbond size of the RTA panels after one cycle was likely smaller than that from the RTW panels because the non-aged material behaved more brittle during pre-cracking. This can be concluded from the more jagged behavior of the RTA panels in Fig. 9, which indicates shock wise crack growth. Furthermore, the load required to start disbond growth during pre-cracking was significantly lower for the RTW panels than for the RTA ones. This indicates a decrease in fracture toughness at the crack initiation point.

The fact that the initiation fracture toughness decreased, whereas it has been mentioned before that the propagation fracture toughness increased, can possibly be explained by the way in which the bond is exposed to the humid environment. The original crack tip had been exposed to four edges, two of which were directly exposed to the hot and humid environment. However, as the crack grew, it encountered material that had only been exposed to two indirect edges at the time of conditioning, which made it harder for the moisture to penetrate. Halliday et al. [31] proved that this causes the fracture toughness at the crack initiation point to be affected differently by hygrothermal aging than the crack propagation fracture toughness.

### 4.2. Stiffness

At set intervals a monotonic test was performed to determine whether cyclic loading and correlated disbond growth had influenced

the stiffness of the panels. Fig. 10 shows a representative example of the load shortening curves of one panel throughout the testing phase.

The fact that cyclic loading did not lead to stiffness losses is in line with the results obtained by Abramovich and Weller [16]. It confirms that the disbond size has limited influence on the stiffness of the panel, as previously suggested in references [8,9,14]. Moreover, it is an indication that if any intralaminar or translaminar damage was present in the panel its influence was limited.

## 5. Quasi-static compression

### 5.1. Buckling load

An overview of the buckling loads of the RTA, RTW and reference panels can be seen in Table 2. It turned out that hygrothermal aging did not significantly influence the buckling load of the panels. This was likely due to the direct relation between the buckling load and stiffness. The stiffness is dominated by the carbon fibers which are not affected by the presence of moisture [34]. Furthermore, for the set-up used in this work the observed buckling shape of the aged and non aged panels were similar. The effect of the internal load redistribution due to moisture uptake is low, as the strain levels due to hygrothermal ageing are low. This is confirmed by a study of Emam and Eltaher [35].

On the other hand, cyclic loading did influence the buckling load of the panels, as demonstrated by the fact that the buckling load of the cyclically loaded panels was 28% lower than that of the reference panels. This could be related to two factors:
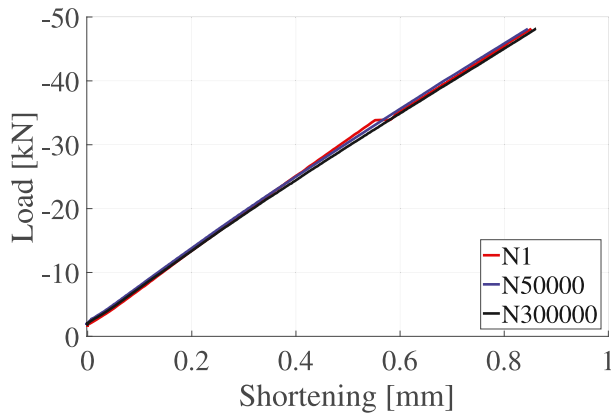
**Fig. 10.** Typical load-shortening curve throughout the cyclic loading experiments.

**Table 2**
Disbond lengths and buckling loads of the quasi-static experiments. *The reference panels were not cyclically loaded.*

|  | Average disbond length [mm] | Average buckling load [kN] |
|---|---|---|
| RTA panels | 112.6 | −16.3 |
| RTW panels | 115.9 | −16.4 |
| Reference panel RTA | 107.9 | −22.7 |
| Reference panel RTW | 107.3 | −22.8 |

1. Larger disbond size of the cyclically loaded panels
2. Local decrease in stiffness due to the cyclic out-of-plane bending

Firstly, due to the disbond growth that occurred during cyclic loading, the cyclically loaded panels had a larger disbond at the onset of the quasi-static experiments than the reference panels. A numerical linear buckling analysis confirmed that for this case a larger disbond could indeed have decreased the buckling load by roughly 3.5%. The fact that the experimental buckling load decreased by 28% has indicated that the influence of the disbond size is limited.

Secondly, cyclic out-of-plane bending can cause a decrease in the out-of-plane bending stiffness [36]. Due to repeated bending of the skin in the disbonded area this can occur locally in the skin without influencing the overall stiffness of the panel against compression. Since the C-scanning device could only pick-up disbonding, it was not possible to verify whether this had indeed happened locally in the disbonded area. However, a linear buckling analysis did confirm that a local decrease in out-of-plane buckling stiffness in the disbonded area could have caused a decrease in buckling load similar to the one presented in this study.

*5.2. Compression stiffness and residual strength*

The hygrothermal aging did not significantly influence the stiffness and strength of the panels after cyclic loading. These conclusions are based on the unchanged membrane strain in the stiffener, which can be seen in Fig. 11. Before collapse, the RTA panels withstood on average −119 kN and the RTW panels −117.3 kN.

The limited influence of hygrothermal aging on the strength and stiffness of the panels, even after cyclic loading, has probably been due to the dominance of the fiber and fiber matrix interface on these properties. Both the fiber and fiber matrix interface are not influenced significantly by moisture [34].

A comparison of the cyclically loaded panels to the reference panels is shown in Fig. 12. This figure shows the load shortening of one typical RTA and RTW panel as well as the reference panels. Because of malfunctioning of one strain gauge in the RTA reference panel during testing, the load shortening curves are shown here instead of the membrane strain.
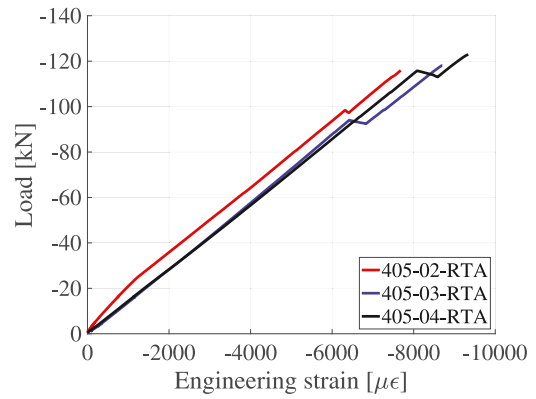


(a) RTA panels
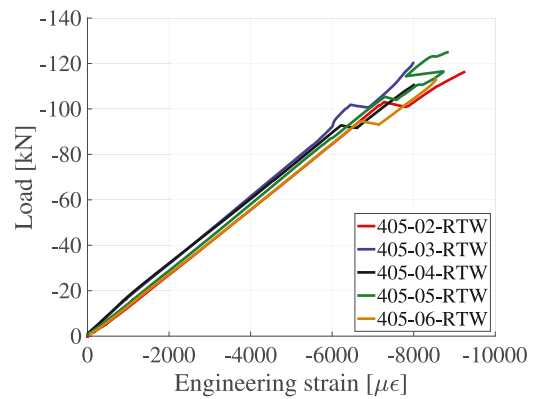


(b) RTW panels

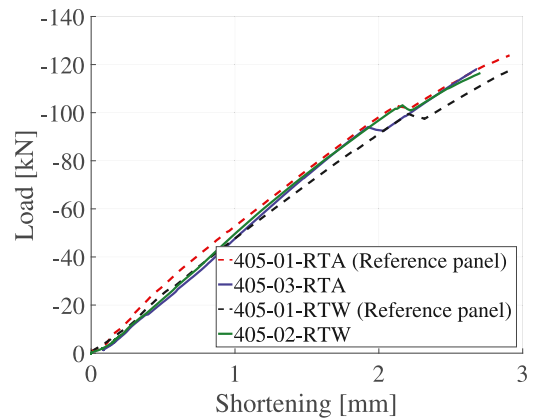**Fig. 11.** Membrane strain in the stiffener as a function of the load.



**Fig. 12.** Typical load shortening curves of the quasi-static residual strength tests and ultimate strength tests of the reference panels.

Based on Fig. 12, cyclic loading had no significant influence on the overall strength and stiffness of the panels. This is in line with the research performed by Davila and Bisagni [15] and Abramovich and Weller [16] and can, at least partially, be explained by the limited amount of disbond growth during the cyclic loading: 100–300 mm$^2$ in comparison to an original disbond size of at least 6400 mm$^2$. This amounted to 1.5–4.5% growth in comparison to the original size. The constant strength and stiffness could be an indication that no significant intralaminar and translaminar damage had occurred.

An impression of the panels after failure can be seen in Fig. 13. All panels failed by either complete disbonding, or locally in the skin
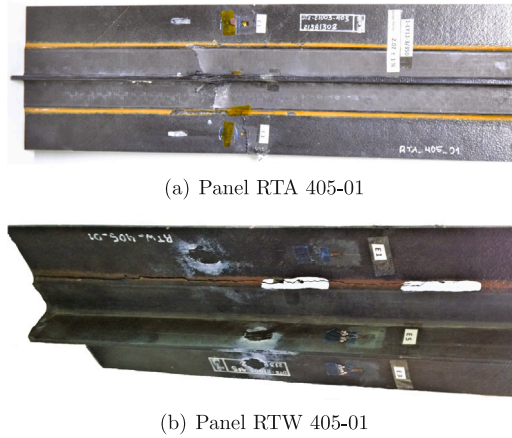
(a) Panel RTA 405-01



(b) Panel RTW 405-01

**Fig. 13.** Examples of a local failure in stiffener/skin (top) complete disbonding. Panel RTW 405-01.

and stiffener. The type of failure was randomly distributed among the RTA/RTW panels and cyclically loaded/reference panels. This indicates that aging and cyclic loading had not influenced the way in which the panels had failed. Analyses on post-mortem specimens showed that most of the tested panels disbonded within the adhesive layer. This has been classified as cohesive failure according to the ASTM D5573 [37] standard.

## 6. Numerical model

A numerical model of both cyclic loading and quasi-static compression until failure was created with Abaqus CAE™ 6.14–1 finite element software. Due to limited availability of the material properties of the RTW panels only the RTA panels were simulated.

An overview of how the geometry of the panels was modeled in Abaqus can be seen in Fig. 14. A separate interface layer of cohesive elements was used to model the adhesive. Thereafter, tie constraints, with the skin and stiffener serving as master surfaces, were applied to connect the interface to the CFRP parts. The cohesive elements can loose their stiffness, which gives a similar type of failure for adhesive and cohesive failure of the interface. To prevent interpenetration, a general surface contact between the skin and stiffener's flange was used.

Elements of 0.4 × 0.4 mm were used in the first 10 mm of the disbond-bond interface. This fine discretization was mainly required to accurately model the disbond growth during the cyclic loading. After 10 mm, a transition similar to the one used by [38] had been applied to increase the mesh size gradually. This resulted in 3.2 × 5 mm sized elements at the ends of the panel. These element sizes were deemed suitable after a careful mesh convergence analysis was performed, requiring less than 1% difference in the disbond growth and maximum load at failure

### 6.1. Interface damage model

The damage in the interface layer, also referred to as disbonding, was modeled by using the cohesive zone model developed by Oliveira et al. [22]. This model has demonstrated that it is able to simulate static and high cycle fatigue damage at coupon level accurately, as well as efficiently [22]. The constitutive law for the cohesive zone model has been defined in terms of a bi-linear traction-separation relationship between two adjacent layers, given as follows:

$$\begin{aligned}
\sigma_I &= K_I(1 - D_K)\langle\delta_I\rangle - K_I\langle-\delta_I\rangle \\
\sigma_{II} &= K_{II}(1 - D_K)\delta_{II} \\
\sigma_{III} &= K_{III}(1 - D_K)\delta_{III}
\end{aligned} \tag{2}$$

where the subscripts $I$, $II$, $III$ refer to the pure disbonding modes ($I = 33$, $II = 13$, $III = 23$), $\sigma_i$ are the respective stresses associated with each disbonding mode acting on the interface, $K_i$ are the interface stiffnesses associated with each disbonding mode, $\delta_i$ are the respective relative displacements between two adjacent layers and $\langle\cdot\rangle = \max(\cdot, 0)$ are the Macaulay brackets. The stiffness damage variable $D_K$ has been calculated from the strength damage variable $D_S$ as follows:

$$D_K(n) = 1 - \frac{\delta_0(1 - D_S)}{\delta_0 + D_S^s(\delta_f - \delta_0)} \tag{3}$$

where $\delta_0$ and $\delta_f$ are the displacements at crack initiation and at element failure. These have been obtained from a stress based criterion proposed by Ye [39] and an energy based criterion proposed by Benzeggagh and Kenane [40]. Further details about the expressions for $\delta_0$ and $\delta_f$ can be found in Ref. [22]. $D_S^s$ is the quasi-static damage parameter, which together with the fatigue damage parameter $D_S^f$ forms the strength damage variable $D_S$:

$$D_S = D_S^s + D_S^f(n) \tag{4}$$

where $n$ refers to the current number of cycles. The expression for the quasi-static damage parameter is given by

$$D_S^s = \left(\frac{\bar{\delta} - \delta_0}{\delta_f - \delta_0}\right) \tag{5}$$

$\bar{\delta}$ is the magnitude of the resultant displacement vector for mixed-mode loading, defined as

$$\bar{\delta} = \left(\langle\delta_I\rangle^2 + \delta_{II}^2 + \delta_{III}^2\right)^{1/2} \tag{6}$$

The expression for the fatigue damage parameter has been based on the work of Kawashita and Hallett [21] and is given by:

$$D_S^f(n) = D_S^f(n - \Delta n) + \Delta D_S^f \tag{7}$$

with

$$\Delta D_S^f = \frac{\Delta n(1 - D_S^s)}{l_{el,\phi}} C\left(\frac{G_{max}(1 - R^2)}{G_c}\right)^m \tag{8}$$

$\Delta n$ is the cycle increment; $R = G_{min}/G_{max}$; $C$ and $m$ are the Paris Law parameters defined in terms of the empirical model proposed by Blanco et al. [41] for mixed-mode loading; and $l_{el,\phi}$ is the effective element length.

To reduce the computational cost, the envelope approach [38] has been used. In this approach only the maximum load is computed and the minimum load is estimated by the load ratio $R$. In this case all the local load ratios were assumed to be equal to the applied ratio. In the present work a small load ratio was applied ($R = 0.1$). Since this results in a negligible minimal load in the entire structure, it is a justified approach. However, more accurate results could be obtained by computing the load ratio locally, as proposed in [42,43], which is particularly important for higher load ratios in the post-buckling regime.

More in depth information of the damage model can be found in the work of Oliveira et al. [22]. The cohesive zone based damage model has been implemented in Abaqus as a user-defined material model in eight node brick elements with reduced integration. Eight node brick elements have been used because twenty node quadratic brick elements were not available in Abaqus Explicit.

### 6.2. Intralaminar damage model

Linear shell elements with reduced integration were applied to model the laminates. The damage itself was modeled using Hashin's damage model [44,45], which had already been available in Abaqus and primarily intended for fiber reinforced polymers [46]. However, as it could only model static damage, it did not take the cyclic loading damage in the CFRP into account. It was already shown in Section 5 that fatigue damage in the CFRP did not influence the overall stiffness and strength of the panel.
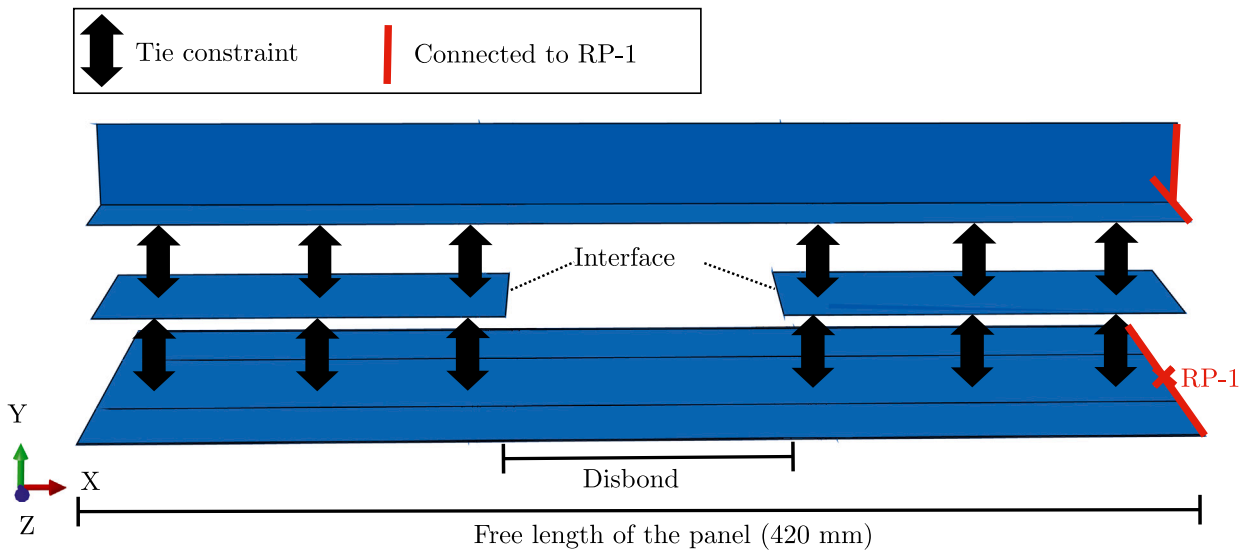
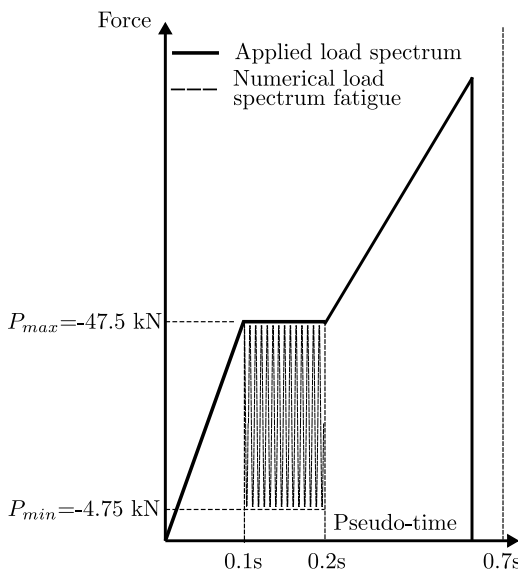**Fig. 14.** Overview of the geometry in the numerical model.



**Fig. 15.** Numerical load applied for the fatigue and residual strength simulations.

### 6.3. Finite element simulation

The simulation was performed using the dynamic explicit solver through the dynamic relaxation method, with geometrical non-linearities activated. To speed up the simulation mass scaling was applied. A target stable time increment of $10^{-6}$ seconds was used, as this resulted in high computational speed, while keeping the kinetic energy below a set criterion of less than 10% of the total energy. Moreover, several stable time increments were tested and compared with respect to disbond growth, failure mode and maximum load at failure. For this simulation no artificial damping was required.

The load was applied in three steps. Step one, lasting 0.1 pseudo second, was to gradually build up the load from 0 to $-47.5$ kN. During the second step the load was kept constant for 0.1 pseudo seconds. Meanwhile, a numerical frequency of 3,000,000 Hz was applied to simulate cyclic loading. The last step served to simulate quasi static compression until failure, during which compression load was applied under displacement control over the course of 0.5 pseudo seconds.

These steps are displayed in Fig. 15. All relevant material properties as used in the numerical simulation are given in Appendix B.

## 7. Numerical results

As a first check, the numerical buckling shape as shown in Fig. 16, was compared to the buckling shape observed by the DIC set-up, as presented in Fig. 7. Unfortunately, the use of a 2D DIC set-up in combination with 3D effects had eliminated the possibility of a quantitative comparison. Therefore, it can only be said that both displayed a similar diagonal buckling shape.

A comparison of the numerical and experimental disbond growth over the course of 300,000 cycles can be seen in Fig. 17. To be in line with the experiments, the disbond growth was measured from the first cycle onward.

It turned out that the growth of the disbonded area of the numerical model matched well with the experiments. After 300,000 cycles the difference was roughly 13%. Furthermore, the growth rate throughout the simulation corresponded well to the experiments. One of the main differences came from the fact that the numerical disbond had grown more diagonal than the experimental disbond, as can be seen by comparing the experimental disbond displayed in Fig. 8 and the numerical disbond in Fig. 18.

The reliability of the numerical model can be further improved by ensuring all material input parameters are known beforehand. Unfortunately, the Paris law parameters and the B–K interpolation exponent of the threshold strain energy release rate ($G_{th}$) from the material combination used in the present research were not known prior to simulation. Instead, both parameters had to be obtained from co-cured HTA/6376C [41,47]. This material was chosen because it had the most similar strain energy release rate properties $G_{I,th}, G_{II,th}, G_{I,c}$ and $G_{II,c}$ for which the Paris law parameters and B–K interpolation exponent were available in open literature. Furthermore, the static strength of the interface layer was also not known prior to modeling. After calibration the static shear strength of the adhesive EA 9695 was used as the static interface strength of the model.

Fig. 19 compares the membrane strain in the stiffener during the quasi-static compression of the RTA panels to the numerical results. Likewise during the experiments, the cyclic disbond growth did not cause any loss in overall stiffness of the panel. Also the residual load of the numerical panel corresponded well to the experiments.
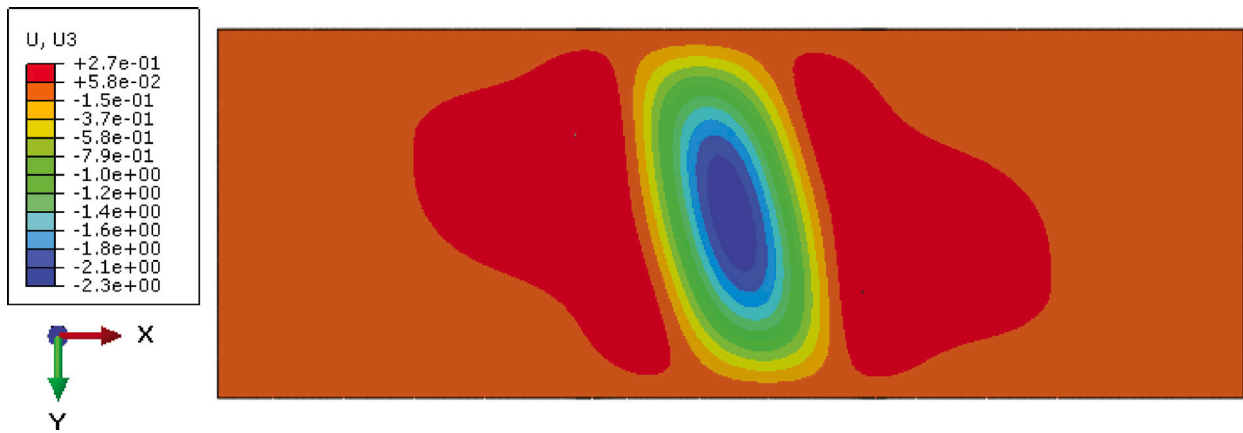
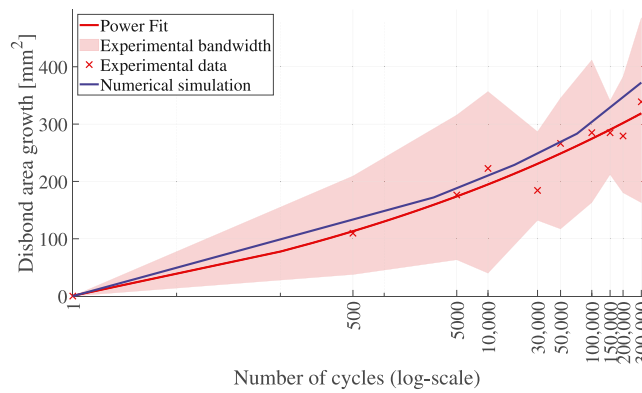**Fig. 16.** Out-of-plane displacement (U3 in mm) in the skin at −47.5 kN.



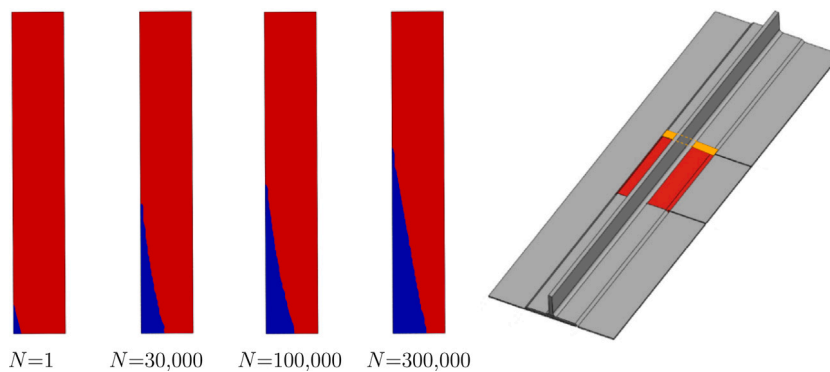**Fig. 17.** Numerical disbond growth.



**Fig. 18.** Left: Numerical disbond shape (blue) after 1, 30,000, 100,000 and 300,000 cycles Right: The location of the bond-disbond interface shown in the left figure is marked orange. (For interpretation of the references to color in this figure legend, the reader is referred to the web version of this article.)

## 8. Conclusions

The present study has confirmed previous research in which hygrothermal aging decreased the fracture toughness at the crack initiation point of bonded composite structures. However, it also demonstrated that moisture uptake can influence the disbond growth of bonded composite panels in a positive way. This is because stress relaxation and crack blunting, both being a result of plasticization, were probably responsible for an increased propagation fracture toughness after moisture uptake. This increase in fracture toughness led to a lower

disbond growth during cyclic compressive loading after hygrothermal aging.

Additionally, the results of the residual strength tests have confirmed earlier research that composite bonded panels with a disbond can safely be taken into the post-buckling regime repeatedly. Moreover, the results of the present study have added to this knowledge by showing that hygrothermally aged co-bonded panels perform equally well after cyclic loading as non aged panels.

Overall, it can be concluded that in the current set-up, being co-bonded parts conditioned up to 396 days, hygrothermal aging did not
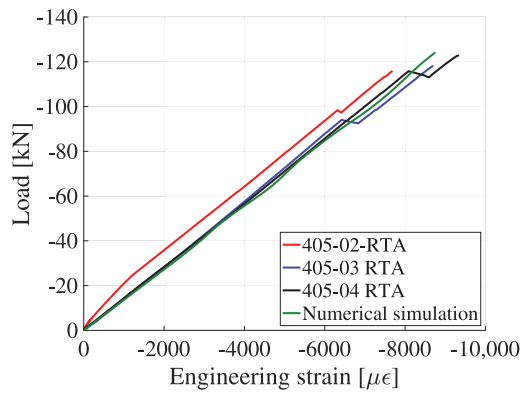
**Fig. 19.** Comparison of the numerical and experimental membrane strain in the stiffener.

negatively influence the lifetime of components during, and after, cyclic loading.

Finally, the present study has also shown that cyclic disbond growth on sub-component level can be modeled efficiently and accurately with the applied cohesive zone model. This can aid the aircraft industry in the prediction of disbond growth in structural parts, as required by the slow crack growth approach proposed by the FAA [23].

Factors such as the used material, lay-up configuration and the bonding method are likely to have influenced how the structure reacted to moisture exposure and cyclic loading. Therefore, it is recommended to further investigate how sensitive the conclusions taken from the present research are to these parameters. Moreover, the current boundary conditions, in the form of anti-buckling supports, limited the out-of-plane displacement of the buckled skin. Removing these supports would increase the out-of-plane displacement and therefore likely the total disbond growth. It is recommended to further investigate the influence of this on the behavior of the panels as well. Lastly, it is recommended to further validate the numerical model decreasing the uncertainties in the material parameters. In the present study the Paris parameters and B–K interpolation coefficient were not known before the start of the modeling, instead values were used from a material with similar fatigue behavior.

**Declaration of competing interest**

The authors declare that they have no known competing financial interests or personal relationships that could have appeared to influence the work reported in this paper.

**CRediT authorship contribution statement**

**Bart P.H. van den Akker:** Writing - original draft, Investigation, Formal analysis, Visualization. **Mauricio V. Donadon:** Resources, Supervision, Methodology, Writing - review & editing. **Richard Loendersloot:** Supervision, Writing - review & editing, Validation. **Lucas A. de Oliveira:** Software, Writing - review & editing. **Mariano A. Arbelo:** Supervision, Resources, Validation.

**Table A.3**
Material data sheet — T800-3900-2B pre-preg tape [50,51].

| Description | Parameter | Magnitude | Unit |
| --- | --- | --- | --- |
| **Strength** | | | |
| Tensile | $S_1^T$ | 2793 | MPa |
| Tensile | $S_2^T$ | 36 | MPa |
| Compression | $S_1^C$ | 1432 | MPa |
| Compression | $S_2^C$ | 226.8 | MPa |
| In-plane shear | $S_{12}$ | 63.8 | MPa |
| Intralaminar shear | $S_{13}$ | 88.1 | MPa |
| **Young's modulus** | | | |
| Tensile | $E_1^T$ | 142–173 | GPa |
| Tensile | $E_2^T$ | 7.8–9.6 | GPa |
| Compression | $E_1^C$ | 125–153 | GPa |
| Compression | $E_2^C$ | 9.9–12.1 | GPa |
| In-plane shear | $\mu_{12}$ | 3.5–4.3 | GPa |
| Fracture toughness | | | |
| Tensile | $G_{Ic}^T$ | 165 | N/mm |
| Tensile | $G_{IIc}^T$ | 10 | N/mm |
| Compression | $G_{Ic}^C$ | 25 | N/mm |
| Compression | $G_{IIc}^C$ | 2 | N/mm |
| **Poisson's ratio** | | | |
| Tensile | $\nu_{12}^T$ | 0.343 | – |
| Tensile | $\nu_{21}^T$ | 0.024 | – |
| Compression | $\nu_{12}^C$ | 0.339 | – |
| Compression | $\nu_{21}^C$ | 0.015 | – |
| **Other** | | | |
| Glass transition temperature | $T_g$ | 166–204 | °C |
| Density | $\rho$ | $1.58 \cdot 10^{-9}$ | ton/mm³ |

With $_1$ being the fiber direction, $_2$ the in plane direction perpendicular to the fibers and $_3$ the out of plane direction perpendicular to the fibers. $_I$ and $_{II}$ refer to the mode I and II opening respectively.

**Table A.4**
Material data sheet adhesive EA 9695 [52].

| Description | Parameter | Magnitude | Unit |
| --- | --- | --- | --- |
| Normal strength | $S_1$ | 6.9 | MPa |
| Shear strength | $S_2 = S_3$ | 31 | MPa |
| Young's modulus | $E$ | 3100 | MPa |
| Glass transition temperature | $T_g$ | 95–150 | °C |
| Poisson's ratio | $\nu$ | 0.33 | – |

**Table A.5**
Mixed mode fracture toughness parameters as obtained from [48] and [49].

| Description | Parameter | Magnitude | Unit |
| --- | --- | --- | --- |
| Mode I fracture toughness | $G_{Ic}$ | 0.235 | N/mm |
| Mode II fracture toughness | $G_{IIc}$ | 6.961 | N/mm |
| B–K mixed mode interpolation coefficient | $\eta$ | 8.48 | – |

**Appendix A. Material properties**

The material properties of the T800-3900-2B tape, as obtained from Toray, are given in Table A.3. Table A.4 contains the material properties of adhesive EA 9695 as obtained from Henkel. Lastly, the mixed mode fracture toughness of the interface layer was previously determined by Brito [48] and Brito et al. [49] and are given in Table A.5.

**Appendix B. Input parameters numerical model**

The material properties that were not exactly defined (CFRP) or were determined through calibration (strength of the interface layer)

**Table B.6**
Material properties of the CFRP as used in the numerical model [50,51].

| Parameter | Magnitude | Unit |
|---|---|---|
| $E_1$ | 125 | GPa |
| $E_2$ | 9.9 | GPa |
| $\mu_{12}$ | 3.5 | GPa |
| $\nu_{12}$ | 0.34 | – |

**Table B.7**
Strength of the interface layer as used in the numerical model, based on the static shear strength of the adhesive: EA 9695 [52].

| Parameter | Magnitude | Unit |
|---|---|---|
| $S_{33}$ | 31 | MPa |
| $S_{12}$ | 31 | MPa |
| $S_{23}$ | 31 | MPa |

**Table B.8**
Additional material properties in the interface layer as required by the cohesive zone model.

| Description | Parameter | Magnitude | Unit |
|---|---|---|---|
| Element size along crack direction | $l_e$ | 0.2 | mm |
| Mode I Paris constant | $C_I$ | 0.00221[a] [41] | – |
| Mode I Paris exponent | $n_I$ | 5.09[a] [41] | – |
| Mode II Paris constant | $C_{II}$ | 0.122[a] [41] | – |
| Mode II Paris exponent | $n_{II}$ | 4.38[a] [41] | – |
| Mixed mode Paris interpolation constant | $C_b$ | 609,000[a] [41] | – |
| Mixed mode Paris interpolation exponent | $n_b$ | 5.48[a] [41] | – |
| Fatigue threshold value mode I | $G_{I,th}$ | 0.0627[b] [53] | N/mm |
| Fatigue threshold value mode II | $G_{II,th}$ | 0.0593[b] [53] | N/mm |
| B–K interpolation exponent for $G_{th}$ | $n_{b,th}$ | 2.737[c] [47] | – |

[a]Obtained from co-cured HTA/6376C [41].
[b]Obtained from coupon level experiments of a previous test campaign [53].
[c]Obtained from co-cured HTA/6376C [47].

are given in Tables B.6 and B.7. The cohesive zone model also required additional input parameters for the interface layer which had not yet been mentioned in Appendix A. These parameters are given in Table B.8.

## References

[1] Stevens K, Ricci R, Davies G. Buckling and postbuckling of composite structures. Composites 1994;26(3):189–99. http://dx.doi.org/10.1016/0010-4361(95)91382-F.

[2] Zhao W, Kapania R. Buckling analysis of unitized curvilinearly stiffened composite panels. Compos Struct 2016;135:365–82. http://dx.doi.org/10.1016/j.compstruct.2015.09.041.

[3] Aslan Z, Sahin M. Buckling behavior and compressive failure of composite laminates containing multiple large delaminations. Compos Struct 2009;89(3):382–90. http://dx.doi.org/10.1016/j.compstruct.2008.08.011.

[4] Wang X, Cao W, Deng C, Wang P, Fue Z. Experimental and numerical analysis for the post-buckling behavior of stiffened composite panels with impact damage. Compos Struct 2015;133:840–6. http://dx.doi.org/10.1016/j.compstruct.2015.08.019.

[5] Kong C, Lee I, Kim C, Hong C. Postbuckling and failure of stiffened composite panels under axial compression. Compos Struct 1998;42(1):13–21. http://dx.doi.org/10.1016/S0263-8223(98)00044-0.

[6] Falzon B, Stevens K, Davies G. Postbuckling behaviour of a blade-stiffened composite panel loaded in uniaxial compression. Composites A 2000;31(5):459–68. http://dx.doi.org/10.1016/S1359-835X(99)00085-8.

[7] Meeks C, Greenhalgh E, Falzon B. Stiffener debonding mechanisms in postbuckled CFRP aerospace panels. Composites A 2005;36(7):934–46. http://dx.doi.org/10.1016/j.compositesa.2004.12.003.

[8] Bisagni C, Davila C. Experimental investigation of the postbuckling response and collapse of a single-stringer specimen. Compos Struct 2014;108:493–503. http://dx.doi.org/10.1016/j.compstruct.2013.09.018.

[9] Orifici A, Ortiz de Zarata Alberdi I, Thomson R, Bayandor J. Compression and post-buckling damage growth and collapse analysis of flat composite stiffened panels. Compos Sci Technol 2008;68(15–16):3150–60. http://dx.doi.org/10.1016/j.compscitech.2008.07.017.

[10] Bisagni C, Vescovini R, Dávila C. Single-stringer compression specimen for the assessment of damage tolerance of postbuckled structures. J Aircr 2011;48(2):495–502. http://dx.doi.org/10.2514/1.C031106.

[11] Sellitto A, Riccio A, Russo A, Zarrelli M, Toscano C, Lopresto V. Compressive behaviour of a damaged omega stiffened panel: Damage detection and numerical analysis. Compos Struct 2019;209:300–16. http://dx.doi.org/10.1016/j.compstruct.2018.10.105.

[12] Modelling the damage evolution in notched omega stiffened composite panels under compression. Composites B 2017;126:60–71. http://dx.doi.org/10.1016/j.compositesb.2017.05.067.

[13] Russo A, Sellitto A, Saputo S, Acanfora V, Riccio A. Cross-influence between intra-laminar damages and fibre bridging at the skin-stringer interface in stiffened composite panels under compression. Mater (Basel, Switzerland) (11):1856. http://dx.doi.org/10.3390/ma12111856.

[14] Yap J, Scott M, Thomson R, Hachenberg D. The analysis of skin-to-stiffener debonding in composite aerospace structures. Compos Struct 2002;57(1–4):425–35. http://dx.doi.org/10.1016/S0263-8223(02)00110-1.

[15] Davila C, Bisagni C. Fatigue life and damage tolerance of postbuckled composite stiffened structures with initial delamination. Compos Struct 2017;161:73–84. http://dx.doi.org/10.1016/j.compstruct.2016.11.033.

[16] Abramovich H, Weller T. Repeated buckling and postbuckling behavior of laminated stringer-stiffened composite panels with and without damage. Int J Struct Stab Dyn 2010;10(04):807–25. http://dx.doi.org/10.1142/S0219455410003750.

[17] Pantelakis S, Tserpes K. Adhesive bonding of composite aircraft structures: Challenges and recent developments. Sci China Phys Mech Astron 2014;57(1):2–11. http://dx.doi.org/10.1007/s11433-013-5274-3.

[18] Budhe S, Banea M, de Barros S, da Silva L. An updated review of adhesively bonded joints in composite materials. Int J Adhes Adhes 2017;72(October):30–42. http://dx.doi.org/10.1016/j.ijadhadh.2016.10.010.

[19] Feng Y, He Y, An T, Cui R, Shao Q, Fan C. Effect of hygrothermal condition on buckling and post-buckling performance of CCF300/5228A aero composite stiffened panel under axial compression. J Reinf Plast Compos 2015;34(12):989–99. http://dx.doi.org/10.1177/0731684415585381.

[20] Song M-G, Kweon J-H, Choi J-H, Byun J-H, Song M-H, Shin S-J, et al. Effect of manufacturing methods on the shear strength of composite single-lap bonded joints. Compos Struct 2010;92(9):2194–202. http://dx.doi.org/10.1016/j.compstruct.2009.08.041.

[21] Kawashita LF, Hallett SR. A crack tip tracking algorithm for cohesive interface element analysis of fatigue delamination propagation in composite materials. Int J Solids Struct 2012;49(21):2898–913. http://dx.doi.org/10.1016/j.ijsolstr.2012.03.034.

[22] Oliveira LAD, Alves DS, Donadon MV. Modelling of mixed mode fatigue-induced delamination in composites : A comparative study. In: 31st congress of the internation council of the aeronautical sciences, Belo Horizonte; 2018, p. 1–9.

[23] Federal Aviation Administration. Aging airplane program: Widespread fatigue damage; Final rule. Fed Regist 2010;75(219):69745–89.

[24] ASTM International. Standard test method for moisture absorption properties and equilibrium conditioning of polymer matrix composite materials BT. 2014.

[25] Gonzalez Ramirez F. Hygrothermal effects on the fatigue delamination growth onset in composite joints. Instituo Tecnologico de Aeronautica; 2018.

[26] Van Rijn J, Wiggenraad J. A seven-point bending test to determine the strength of the skin-stiffener interface in composite aircraft panels. Tech. rep., NLR; 2000.

[27] Hottentot Cerderlof D. Durability of sitffened CFRP panels with initial delaminations. Technische Universiteit Delft; 2018.

[28] Hu P, Lundquist E, Batdorf S. Effect of small deviations from flatness on effective width and buckling of plates in compression. Tech. rep., Langley Field: NACA; 1946.

[29] Singer J, Arbocz J, Weller T. Buckling experiments : experimental methods in buckling of thin-walled structures. Wiley; 1998, p. 1732.

[30] Blaber J, Adair B, Antoniou A. Ncorr: Open-source 2D digital image correlation matlab software. Exp Mech 2015;55(6):1105–22. http://dx.doi.org/10.1007/s11340-015-0009-1.

[31] Halliday S, Banks W, Pethrick R. Dielectric studies of adhesively bonded CFRP/epoxy/CFRP structures - design for ageing. Compos Sci Technol 2000;60(2):197–207. http://dx.doi.org/10.1016/S0266-3538(99)00111-6.

[32] Hutchinson A, Hollaway L. Environmental durability. Strengthening of reinforced concrete structures. Elsevier; 1999, p. 156–82. http://dx.doi.org/10.1533/9781855737617.156.

[33] Packham D. Handbook of adhesion. John Wiley and Sons; 2005, p. 638.

[34] Sciolti MS, Frigione M, Aiello MA. Wet lay-up manufactured FRPs for concrete and masonry repair: influence of water on the properties of composites and on their epoxy components. J Compos Constr 2010;14(6):823–33. http://dx.doi.org/10.1061/(ASCE)CC.1943-5614.0000132.

[35] Emam S, Eltaher M. Buckling and postbuckling of composite beams in hygrothermal environments. Compos Struct 2016;152:665–75. http://dx.doi.org/10.1016/j.compstruct.2016.05.029.

[36] Van Paepegem W, Degrieck J. Experimental set-up for and numerical modelling of bending fatigue experiments on plain woven glass/epoxy composites. Compos Struct 2001;51(1):1–8. http://dx.doi.org/10.1016/S0263-8223(00)00092-1.

[37] ASTM D5573-99, Standard practice for classifying failure modes in fiber-reinforced plastic (FRP) joints. ASTM International; 2019, http://dx.doi.org/10.1520/D5573-99R19.

[38] Peerlings R, Brekelmans W, de Borst R, Geers M. Gradient-enhanced damage modelling of high-cycle fatigue. Internat J Numer Methods Engrg 2000;49(12):1547–69. http://dx.doi.org/10.1002/1097-0207(20001230)49:12<1547::AID-NME16>3.0.CO;2-D.

[39] Ye L. Role of matrix resin in delamination onset and growth in composite laminates. Compos Sci Technol 1988;33(4):257–77. http://dx.doi.org/10.1016/0266-3538(88)90043-7.

[40] Benzeggagh M, Kenane M. Measurement of mixed-mode delamination fracture toughness of unidirectional glass/epoxy composites with mixed-mode bending apparatus. Compos Sci Technol 1996;56(4):439–49. http://dx.doi.org/10.1016/0266-3538(96)00005-X.

[41] Blanco N, Gamstedt E, Asp L, Costa J. Mixed-mode delamination growth in carbon–fibre composite laminates under cyclic loading. Int J Solids Struct 2004;41(15):4219–35. http://dx.doi.org/10.1016/j.ijsolstr.2004.02.040.

[42] Raimondo A, Bisagni C. Analysis of local stress ratio for delamination in composites under fatigue loads. AIAA J 2020;58(1):455–63. http://dx.doi.org/10.2514/1.J058465.

[43] Zhang B, Kawashita LF, Hallett SR. Composites fatigue delamination prediction using double load envelopes and twin cohesive models. Composites A 2020;129:105711. http://dx.doi.org/10.1016/j.compositesa.2019.105711.

[44] Hashin Z, Rotem A. A fatigue failure criterion for fiber reinforced materials. J Compos Mater 1973;7:448–64.

[45] Hashin Z. Failure criteria for unidirectional fiber composites. J Appl Mech 1980;47(2):329–34.

[46] ABAQUS Inc2014. ABAQUS analysis user's manual. 2014.

[47] Asp L, Sjogren A, Greenhalgh E. Delamination growth and thresholds in a carbon/epoxy composite under fatigue loading. J Compos Technol Res 2001;23(2):55–68. http://dx.doi.org/10.1520/CTR10914J.

[48] Brito C. Hygrothermal effects on interlaminar fracture toughness of composite joints (Msc thesis), Instituto Tecnologico de Aeronautica; 2017.

[49] Brito C, de Cassia Mendonca Sales Contini R, Gouvêa RF, Scaglioni De Oliveira A, Arbelo MA, Donadon MV. Mode i interlaminar fracture toughness analysis of co-bonded and secondary bonded carbon fiber reinforced composites joints. Mater Res 2017;20:873–82. http://dx.doi.org/10.1590/1980-5373-MR-2016-0805.

[50] Toray. 3900 prepreg system. 2017, https://www.toraycma.com/file_viewer.php?id=4866.

[51] Toray, Composite Materials Research Laboratories, http://www.toray.com/technology/organization/laboratories/lab_004.html.

[52] Henkel Adhesives, Hysol EA9695 - Epoxy Film Adhesive, https://tdsna.henkel.com/NA/UT/HNAUTTDS.nsf/web/91BE82408EC0B5558525715C001BD52C/$File/LOCTITEEA9695AERO.PDF.

[53] Garpelli F. Experimental characterization of fatigue delamination growth onset in composite joints tested at room temperature ambient condition (RTA) (Msc thesis), Technological Institute of Aeronautics; 2018.